Separation and Purification Technology 380 (2026) 135302

Contents lists available at ScienceDirect

Separation and Purification Technology

journal homepage: www.elsevier.com/locate/seppur

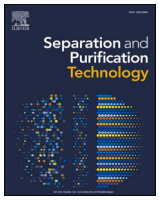

New TiO_2-Ag/BEA composites with dual Ag-functionalization for specific adsorption and catalytic sites. Synergism between phases in the ethylene removal for climateric fruit conservation

Ricardo Ferreira [a], Ana Regadera-Macías [b], Sergio Morales-Torres [b], Luisa M. Pastrana-Martínez [b], João P. Lourenço [a,c], João M. Silva [a,d], Isabel M. João [d,e], M. Filipa Ribeiro [a,*], Auguste Fernandes [a,*], Francisco J. Maldonado-Hódar [b,*]

[a] Centro de Química Estrutural, Institute of Molecular Sciences, Instituto Superior Técnico, Universidade de Lisboa, Lisboa, Portugal
[b] NanoTech – Nanomaterials and Sustainable Chemicals Technologies, Department of Inorganic Chemistry, Faculty of Science, University of Granada, Granada, Spain
[c] Faculdade de Ciências e Tecnologia, Universidade do Algarve, Faro, Portugal
[d] Instituto Superior de Engenharia de Lisboa, Lisboa, Portugal
[e] CEG-IST, Instituto Superior Técnico, Universidade de Lisboa, Lisboa, Portugal

ARTICLE INFO

Keywords:
Photocatalysis
Adsorption
Ethylene
TiO_2
Ag-BEA zeolite

ABSTRACT

A new series of TiO_2-Ag/BEA composites was specifically designed for use in filter/photo-reactors intercalated in air recirculation circuits in storage facilities for climacteric fruits. The sol-gel procedure for TiO_2 deposition was combined with ionic exchange (IE) or incipient wet impregnation (IWI) techniques for Ag doping, with the proportions of both fractions also varying. The prepared materials were thoroughly characterized in terms of their porous texture, chemical composition, crystalline structure, and Ag dispersion, among other properties. Dynamic ethylene adsorption was recorded in the dark. After saturation, ethylene photooxidation was analyzed under UV or UVA-visible light, with varying contact times, flow rates, and concentrations, and with or without humidity present. The maximum ethylene adsorption capacity (361 μmol g^{-1}) corresponds to the sample with the highest Ag content (5 wt%), added by IE, while the best photocatalytic performance is obtained for samples doped by IWI. The performance of the samples was found to be correlated with their physicochemical properties and was specifically determined by the nature and dispersion of the silver species in the composites. Total ethylene photooxidation is achieved even under UV–Vis radiation; the reaction develops selectively to CO_2 in all cases, despite the strong negative effect of humidity on the formation of more active HO• radicals. The high adsorption capacity and effective photooxidation of ethylene enable control of this maturation hormone below the established limits.

1. Introduction

The production of fruits and vegetables is essential for the Mediterranean economy. Moreover, ensuring the availability of these foods beyond their natural season is essential for maintaining a healthy diet within the population. Almost all the fruits and vegetables consumed in the EU are from this region. As such, reducing waste production is a major concern for fruit producers. One crucial problem that fruit producers face is the ripening and, ultimately, senescence of fruits during storage in chambers. This makes the final product undesirable for the consumers and should be discarded, with the consequent economic loss. Ripening is catalyzed by ethylene (C_2H_4), which is emitted by the fruit itself and works as a natural hormone that accelerates the growth of plants or the maturation of the fruits [1]. Removing this hormone is therefore extremely important. Several methods can be used to deal with this problem, with the most commonly used in industry being ventilation and chemical inhibition [2]. However, both methods have their drawbacks. First, the use of ventilation still leaves traces of ethylene in the conservation chamber, sufficient to initiate the ripening processes. The use of chemical inhibitors, like 1-MCP, suppresses ripening by

* Corresponding authors.
E-mail addresses: filipa.ribeiro@tecnico.ulisboa.pt (M.F. Ribeiro), auguste.fernandes@tecnico.ulisboa.pt (A. Fernandes), fjmaldon@ugr.es (F.J. Maldonado-Hódar).

https://doi.org/10.1016/j.seppur.2025.135302
Received 11 August 2025; Received in revised form 12 September 2025; Accepted 19 September 2025
Available online 20 September 2025

binding to the ethylene receptors of the fruit. Nevertheless, the use of chemicals in fruits raises strong public resistance [3]. Therefore, it is important to address this issue with other types of ethylene removal methods. One promising method is the photooxidation of ethylene, which is considered highly efficient and cost-effective [4,5]. This method consists of the conversion of ethylene into CO_2 and H_2O in the presence of a catalyst. Using photocatalysts active under solar radiation is one of the most interesting and sustainable technologies.

Different nanostructured semiconductors, mainly based on transition metal oxides (e.g., Fe_3O_4, ZnO, WO_3) or mixed metal-oxides (eg. -$[Bi_xFe_{(1-x)}]_2O_3$ (x = 0.02, 0.05, 0.10, and 0.20) can be employed as suitable photocatalysts [5,6]. Among them, the most common and popular photocatalyst used is TiO_2, due to its unique properties, including non-toxicity, chemical inertness, high stability, and low cost. Nevertheless, TiO_2 presents a high band gap (BG) value, which, together with a limited surface area (poor adsorption capacity) and a fast recombination of photo-induced electron-hole pairs (h^+/e^-), leads to a poor photocatalytic efficiency under solar radiation and to fast catalyst deactivation. To address the limitations of TiO_2, several strategies have been followed by researchers [7–11]. They are based on: i) the modification of the BG values by doping with metal or non-metal heteroatoms, ii) fit the morphology, nanostructure, and crystal size to minimize the h^+/e^- recombination, iii) supporting the semiconductor active phase on porous materials (carbon, zeolites, etc.) to improve the adsorption capacity and minimize crystal growth. A tentative integration of these approaches is undertaken in this work.

Zeolites are microporous materials that are suitable as supports of semiconductors with potential photocatalytic activity, such as TiO_2. In particular, zeolite BEA has been shown to be an interesting option due to its large surface area, which leads to better TiO_2 dispersion and, subsequently, an improved light absorption and ethylene adsorption efficiency [8,12,13]. The h^+/e^- recombination also decreases with the crystal size. Regarding ethylene adsorption, as demonstrated by Ferreira and coworkers [8], despite the high surface value of the raw zeolites, they still present a low ethylene adsorption related to the low interaction of the non-polar ethylene molecules with the charged zeolite surface groups. As a consequence, in supported TiO_2/BEA composites, the presence of zeolite alone is not enough to substantially increase ethylene adsorption of photocatalysts. Nevertheless, this parameter strongly increased after exchanging zeolite with Ag^+ [14]. These results agree with those exposed by several authors, who reported that stabilizing monovalent Ag^+ species into a zeolite framework will increase ethylene adsorption since these species will interact with ethylene via the so-called π complexation mechanism [14–18]. Reversible chemical complexation of ethylene on other metal ionic sites, such as Cu^+, was also described [19].

On the other hand, as commented, one of the classical approaches to improve the photocatalytic performance of TiO_2 is lowering the BG energy by doping with noble metals [5,20]. Ag is a good choice as a dopant of TiO_2 because of its high work function and ability to produce plasmonic effects, allowing the enhancement of visible light absorption through the large surface plasmon resonance (LSPR) effect. The isolated energy level of Ag 4d promotes visible-light absorption, and the Ag-TiO_2 heterojunction improves the effective separation of electrons and holes [21]. The silver nanoparticles work as collector centers for electrons photoinduced in the conduce band (CB) of TiO_2. The different synthetic methodologies also lead to different dispersion and distribution of Ag-species, forming oxides or metallic nanoparticles, thus changing the interaction between phases, which should be optimized. Ag in the form of Ag_2O (band gap of 1.7 eV) can offer an additional advantage for ethylene photooxidation by shifting the light absorption of TiO_2 towards the visible spectrum [22–24].

On this basis, in this work, we used protonic H-BEA as microporous support, TiO_2 semiconductor as photocatalytic phase, and Ag as doping agent. The optimization of materials was carried out by fitting both the TiO_2 and Ag loadings. In addition, two procedures of synthesis were analyzed, paying attention to the interactions between phases and the nature of the TiO_2-Ag heterojunctions. In the first case, the zeolite was exchanged with an Ag^+ solution to improve the adsorption capacity, according to previous results [14]. Then, the TiO_2 phase was also loaded by sol-gel techniques, leading to TiO_2-Ag-BEA systems. In the second case, the TiO_2 phase was directly loaded on the H-BEA zeolite following the same sol-gel procedure, and Ag was finally deposited by the classical incipient wet impregnation technique. These approaches allow us to obtain information on the evolution of textural, morphological, crystal size, or crystallographic phases or optical parameters, which, in turn, justify the performance of the different composites. Results show that improving the adsorption of ethylene, the cumulative ethylene photooxidation is also favored, with the reaction developing without deactivation and selectively converting ethylene to CO_2 via the photo-induced formation of oxidant radical species ($HO^{\bullet}$, $O_2^{\bullet-}$). The presence of humidity strongly limits the photoactivity because of the competitive adsorption of water and ethylene molecules. The best adsorptive and photocatalytic performance is obtained after deposition of Ag-nanoparticles by IWI regarding IE, denoting the different interactions and synergisms between the support-active phase–doping agent obtained depending on the synthesis procedure. These materials offer a clear advantage, associated with their excellent performance as adsorbents and/or photocatalysts (under visible light), whose combination allows for high efficiency in the removal of ethylene in air flows, even at concentrations much higher than those required for the proposed application.

2. Experimental

2.1. Materials and methods

Commercial parent zeolite (NH_4-BEA, Si/Al of 12.5, CP814E) was purchased from Zeolyst. Titanium isopropoxide (97 % *w*/w) and silver nitrate (99 % w/w) were purchased from Sigma Aldrich. NH_4OH (25 vol % NH_3) was obtained from Fluka, while ethanol absolute (99.5 % w/w) was supplied by Honeywell.

2.2. Preparation of ag-BEA

The Ag-based composites were prepared by adapting the procedure described elsewhere [14], in which silver was initially incorporated in the zeolite structure, by ion exchange. The procedure consisted of suspending 2.5 g of zeolite in 250 ml of an aqueous silver nitrate ($AgNO_3$) solution. The mixture was stirred for 24 h at room temperature in the dark. Ion exchange was carried out one or three times using 0.01, 0.015, and 0.03 M solutions of $AgNO_3$ to achieve different Ag contents similar to the ones obtained in our previous work [14]. The suspension was then filtered and washed, using distilled water, and then dried in an oven at 80 °C overnight. The dried material was then calcined at 500 °C in a muffle for 6 h. For comparison purposes, H-BEA was prepared by calcination of 2 g of NH_4-BEA at 500 °C in a muffle furnace for 6 h.

2.3. Preparation of TiO_2-BEA and TiO_2-ag-BEA composites

The procedure used for the preparation of TiO_2-BEA composites can be found in detail elsewhere [8]. Briefly, 1.5 g of Ag-BEA or H-BEA was suspended in an ethanol solution (15 ml) that contained the titanium precursor ($Ti(OCH(CH_3)_2)_4$). The mixture was stirred for 15 min, and then an ammonium hydroxide solution (NH_4OH, 25 % in water) was added dropwise (20 ml, 1 M). After the addition, the suspension was stirred for an additional 3 h. Lastly, the suspension was dried in a rotary evaporator. The fine powder was recovered, grinded, and calcined in a muffle at 450 °C for 4 h (2 °C.min^{-1} heating rate). The exact amount of Ti precursor was chosen to ensure that the TiO_2-BEA composites contained 20 and 30 wt% of TiO_2, respectively, while for the Ag-based composites, the Ti precursor amount was kept the same, which

resulted in composites with 30 wt% of TiO_2. In this case, the silver was previously supported on zeolite as described above. The samples without Ag were designated as $xTiO_2$-BEA, where x represents the TiO_2 content (wt%). For the Ag-based composites, the samples were labelled as $30TiO_2$-yAg-BEA or $30TiO_2$-BEA-yAg, where y indicates the Ag content (wt%) and the order of the components clearly indicates if the zeolite was previously exchanged with Ag by IE or Ag added on the TiO_2-BEA composites by IWI. For comparison, a sample consisting of TiO_2, referred to as TiO_2 bulk, was prepared by the same sol-gel method. Table S1 summarizes the nomenclature and preparation procedure of the samples synthesized.

2.4. Composite characterization

The composites were characterized using several analytical techniques, as reported in our previous work [8]. Powder X-ray diffraction (XRD) was performed using a D8 Advance diffractometer (Bruker) with Cu Kα radiation filtered by Ni and a 1D LynxEye detector. Nitrogen sorption experiments were performed using Autosorb IQ equipment from Quantachrome. Prior to each measurement, the samples were outgassed at 90 °C for 1 h, followed by 350 °C for 5 h. Stoeckli Eqs. [25] were applied to determine the micropore width (L_0). DRS UV–visible spectra were performed with the help of a Praying Mantis diffuse reflectance accessory, coupled to a Cary 5000 spectrophotometer (Varian). The band gaps (E_g) were calculated from the corresponding Tauc plots (indirect method [26]). X-ray photoelectron spectroscopy (XPS) analysis was performed with a Kratos Axis Ultra-DLD to determine the nature and percentage of the chemical species in the composites. High-resolution transmission electron microscopy characterization was conducted in a FEI Titan G2 50–300 kV high-resolution microscope, equipped with an EDX (energy dispersive X-ray) microanalysis system with elemental mapping. The Ag-based composites were additionally characterized by H_2-TPR experiments, using an automated Autochem II 2920 apparatus (Micromeritics). The composites were first pre-treated under Argon (25 $ml.min^{-1}$) at 250 °C for 1 h and then cooled down to RT. After, the samples were heated up to 900 °C (10 $°C.min^{-1}$) under a 5 % H_2/Ar mixture (30 $ml.min^{-1}$). The H_2 consumption was followed by a thermal conductivity detector (TCD).

2.5. Ethylene adsorption and photooxidation experiments

The experimental facility designed for adsorption/photooxidation experiments is shown in Scheme 1. The samples are pre-treated in a muffle at 250 °C for 25 min to remove any adsorbed compound from the surface of the material. Then the composites are loaded into a quartz/glass reactor (0.45 g), operating at atmospheric pressure. The total flow for every experiment was 25 $ml.min^{-1}$ of a mixture of $N_2/O_2/H_2O/C_2H_4$. In general, this flow is adjusted to contain 21 % of O_2 (synthetic air) and 100 ppms of C_2H_4 using N_2 to balance the total flow, although some experiments were conducted with varying concentrations, including the C_2H_4 concentration (200 ppm), O_2 concentration (16 %), and water content (50 % relative humidity). The experimental procedure was reported in detail in [8,10,11,27,28]. Parameters such as column height and width, packing particle size, ethylene concentration, and total flows were previously optimized [28].

Before each photocatalytic reaction, the gas mixture was passed through the sample without light to achieve ethylene adsorption equilibrium. The corresponding breakthrough curve data was recorded and analyzed. Then, the sample was irradiated using a medium-pressure mercury lamp equipped with a cooling jacket. Depending on the material of the cooling jacket – quartz or glass – the experiments were conducted under two different irradiation spectrums – UV–Vis or UVA-Vis, respectively. The glass jacket blocks radiation with wavelengths below 300 nm, while UVA-Vis radiation ($\lambda > 350$ nm) accounted for 74 % of the lamp irradiation power. Each reaction had a total duration of 3 h and 30 min.

During the reaction, the ethylene and CO_2 concentrations were recorded every 6 min. For each point, the ethylene conversion was calculated using eq. (1).

$$C_2H_4\ conversion\ (\%) = \frac{Initial\ C_2H_4\ (ppm) - C_2H_4\ (ppm)}{Initial\ C_2H_4\ (ppm)} \times 100 \quad (1)$$

The Turnover Frequency (TOF) was calculated using the total CO_2 concentration produced, following eq. (2), to assess photocatalytic performance and compare the results between samples.

$$TOF\ (s^{-1}) = \frac{Initial\ C_2H_4\ (g/s) \times \left(\frac{CO_2\ produced\ (ppm)}{2 \times Initial\ C_2H_4\ (ppm)}\right)}{m_{TiO_2}(g)} \quad (2)$$

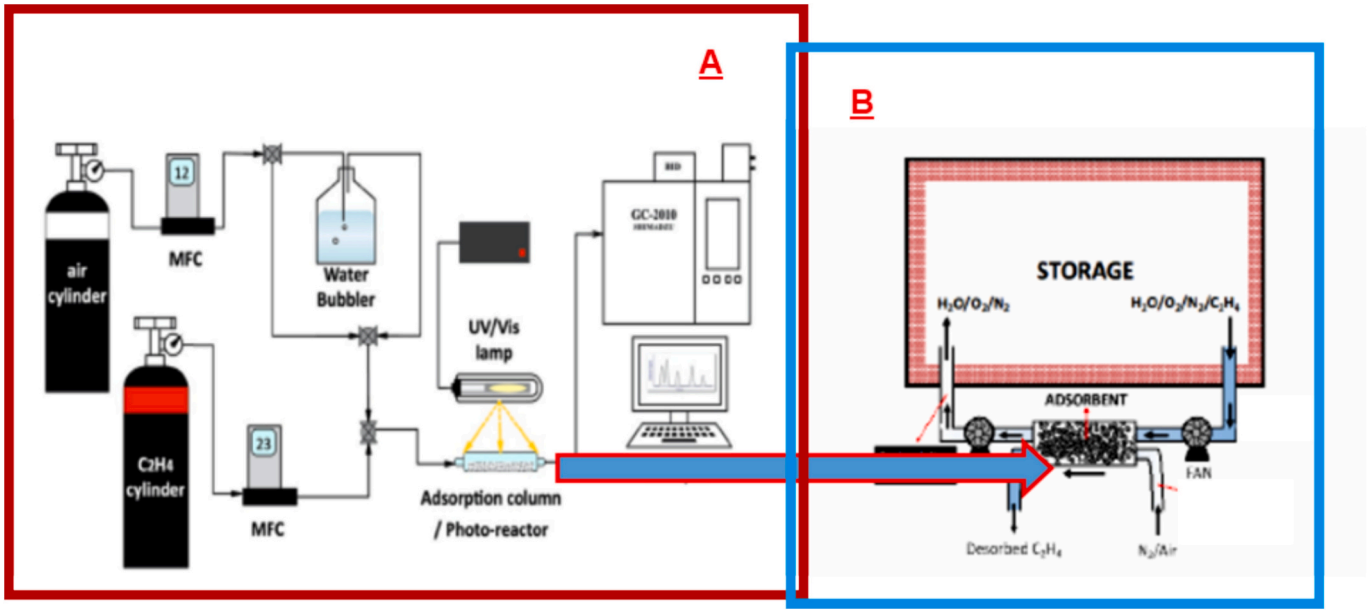

Scheme 1. A) Experimental system used for the dynamic adsorption or photooxidation of ethylene. B) Intercalation of filter/bioreactors in the recirculation air system of the storage refrigerated cameras used for the conservation of fruits.

3. Results and discussion

3.1. Sample characterization

All the samples were exhaustively characterized from different points of view, including textural, morphological, crystallographic, or chemical aspects, before testing as adsorbents or photocatalysts for ethylene removal. Preliminary results obtained by HRSEM (Fig. S1) show the morphology of composites regarding raw zeolite, denoting a more round-shaped distribution of microcrystals and the formation of small aggregates between them.

The analysis of the textural parameters along the sample series provides information about the distribution of supported phases on zeolite porosity. It is well known that the BEA 3D-structure system is formed by 12-membered ring channels with diameters of 0.76 × 0.64 and 0.55 × 0.55 nm, which define the ordered microporous texture of this material. In Table 1, the different parameters are summarized from the analysis of N_2-adsorption isotherms, as BET surface area values, the mean micropore size (L_0), and the quantification of micro/*meso* volumes. The value of L_0 determined for raw BEA zeolite agrees with the published data (0.73 nm). We also obtained the mesopore size distribution by applying the BJH method to the corresponding isotherms, with results shown in Fig. 1. This shows a bimodal mesopore PSD, in which the first small maximum, located for pores with a mean diameter of around 2 nm, is accompanied by another wide and intense peak centred for pores with a diameter of around 20–40 nm. Textural transformations after deposition of TiO_2 phases occur mainly in this porosity range. As observed in Table 1, for TiO_2-BEA composites, microporosity (V_{micro}) is progressively widened with increasing TiO_2 loading (from 20 to 30 wt%), as denoted by the increase of the L_0 values. Since widening cannot be induced by coatings, the results suggest that micropores are progressively blocked, thereby increasing the mean pore size (L_0) accessible to N_2. Simultaneously, the volume of larger mesopores, associated with interparticle voids, also progressively decreases (Fig. 1), while a new peak centred in pores with around 4–5 nm in diameter progressively increases. These results suggest that the TiO_2 phase is deposited inside the large mesopores, narrowing this porosity range, generating narrower mesopores and blocking microporosity. Development of narrow mesopores and blockage of the largest ones increases with the TiO_2 loading.

Nevertheless, if zeolite is exchanged with Ag (ionic exchange – IE samples) before depositing 30 wt% of TiO_2-active phase, the decrease of surface area is stronger and progressive with increasing Ag-loadings, suggesting that Ag can be deposited inside the microporosity since L_0 decreases with high Ag-loadings. However, with increasing Ag-loading, the commented reduction of large mesopores by the TiO_2 deposition is progressively hindered (Fig. 1), and consequently, also a smaller development of narrow mesopores (4 nm). In fact, the transformation of larger into narrower mesopores is even smaller for all the IE Ag-doped composites than for 20TiO_2-BEA. This means that previously exchanged Ag species occupied the raw micro and smaller mesoporosity, forcing the posterior formation of TiO_2 coatings in larger pores, that is, on a more external surface. Due to the smaller development of narrower mesopores, the contribution of the external surface (S_{ext}) is also slightly smaller, and as a consequence, S_{BET} values decreased with increasing Ag-loadings. The previous exchange with Ag leads to a progressive loss of porosity and surface area in the final photocatalysts. The composite with higher Ag and TiO_2 contents showed smaller S_{BET} values and total porosity. Doping 30TiO_2-BEA with Ag at 3.5 wt% by IWI (30TiO_2-BEA-3.5Ag) also produces a significant reduction of porosity. Still, in this case, the deposition of Ag-nanoparticles leads to an additional blockage of the larger mesopores of 30TiO_2-BEA, resulting in a broader distribution of the narrower ones (Fig. 1), which confirms that these Ag-nanoparticles are located on the mesoporous surface in this composite, regarding Ag-species mainly located inside microporous surface when doping by IE, as previously commented.

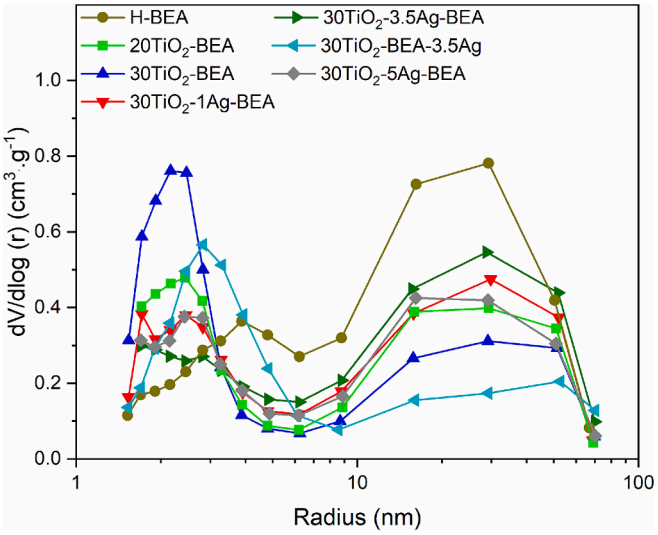

Fig. 1. Pore size distribution curves (BJH, desorption branch) of TiO_2-BEA composites and Ag-based composites.

Table 1
– Textural properties of different composites and the parent zeolite.

Sample	V_{micro} [a]	V_{meso} [b]	S_{ext} [c]	S_{BET} [d]	L_0 [e]
H-BEA	0.17 (100)	0.78	205	627	0.73
20TiO_2-BEA	0.12 (88)	0.54	238	516	0.89
30TiO_2-BEA	0.09 (76)	0.55	314	522	1.02
30TiO_2–1.0Ag-BEA	0.09 (76)	0.52	206	463	0.91
30TiO_2–3.5Ag-BEA	0.10 (77)	0.51	204	414	0.88
30TiO_2-BEA-3.5Ag	0.10 (77)	0.52	180	430	0.93
30TiO_2–5.0Ag-BEA	0.09 (76)	0.42	201	404	0.95

[a] $cm^3.g^{-1}$ (percentage of micropores volume considering the dilution effect of zeolite in the final composite material); [b] $V_{meso} = V_{total} - V_{micro}$; [c] determined from *t*-plot. [d] S_{BET} calculated in the P/P_0 range of 0.05–0.3; [e] calculated through the Stoeckli equation $L_0 = 24/E_0$, with E_0 determined by the DR method.

TEM/EDX mapping was used to analyze the dispersion and distribution of Ag and Ti on the zeolite support; results are shown in Fig. 2. The EDX mapping image for the 30TiO_2-BEA (Fig. 2b) sample shows that Ti is well dispersed and homogeneously covering the particle of support. For the IE Ag-doped composites (Figs. 2c-h), small Ag particles are observed and homogeneously distributed along the samples. EDX mapping confirms that these new particles correspond to Ag-species. The size of these Ag nanoparticles increases as the Ag content increases; the mean diameter is 2.7 nm for 30TiO_2–1.0Ag-BEA but increases up to 6.2 nm for 30TiO_2–5.0Ag-BEA (Fig. S2).

The crystallographic characteristics of the samples were determined by XRD. The diffraction of pure phases is summarized in Fig. 3a. The characteristic peaks of the zeolite BEA structure located at around 2θ of 5 and 23° are clearly observed. The pattern of bulk TiO_2 denotes peaks corresponding exclusively to the anatase phase, the Scherrer equation providing a mean crystallite size of about 11 nm. The XRD patterns of IE Ag-BEA supports, prior to the TiO_2 introduction (Fig. S3), show a small peak at 37° (2θ) corresponding to the (111) plane of cubic Ag^0, more clearly in the samples with higher Ag content (3.5 and 5 wt%). XRD patterns of composites are shown in Fig. 3b. XRD patterns of the composites exhibit the characteristic peaks of both phases, with a relative intensity varying according to TiO_2 concentration. Results confirm the conclusions of previous works [8]. At low TiO_2-loading, the 20TiO_2-BEA diffractogram shows no detectable peaks from TiO_2. Very small crystallites of anatase or amorphous TiO_2 are formed in these experimental conditions on the BEA surface. When TiO_2 loadings increase up to 30 wt

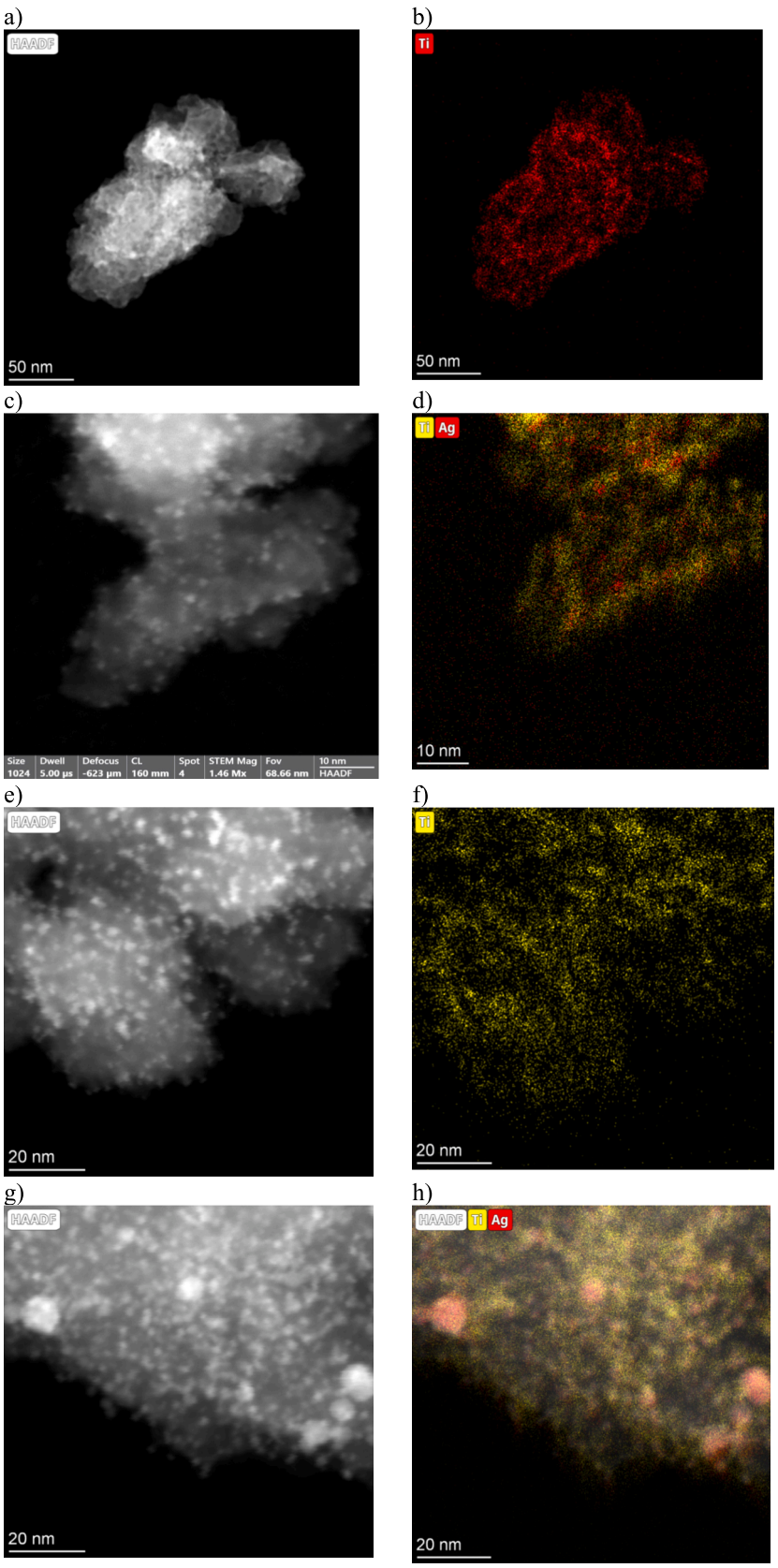

Fig. 2. TEM images a,b) 30TiO_2-BEA, c,d) 30TiO_2–1.0Ag-BEA, e,f) 30TiO_2–3.5Ag-BEA, g,h) 30TiO_2–5.0Ag-BEA and corresponding EDS mapping.

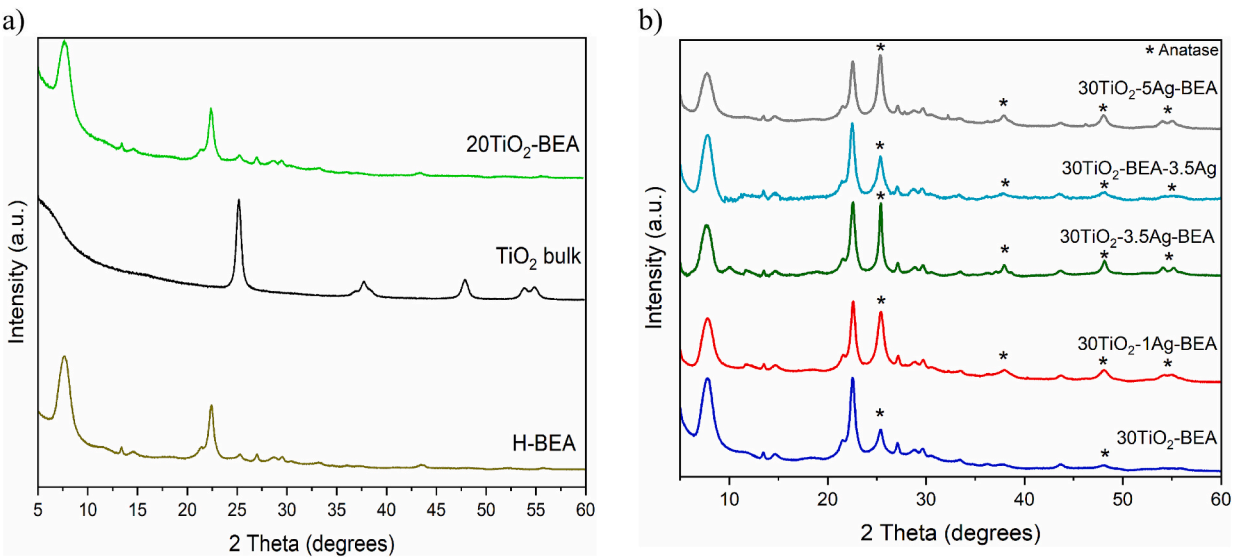

Fig. 3. PXRD patterns of a) parent zeolite, bulk TiO_2 material, and 20TiO_2-BEA; b) 30TiO_2-BEA and Ag-based composites.

% (30TiO_2-BEA, Fig. 3b), the anatase peaks are observed again. In this case, the Scherrer equation indicates the formation of crystallites of 12 nm, which is similar to those found in bulk TiO_2 but highly distributed on the zeolite surface.

When TiO_2 was deposited on Ag-BEA, although the TiO_2 content was maintained at 30 wt%, the intensity of the (101) anatase peak progressively increased (Fig. 3b) with the Ag-loading. The ratio I_{100} (BEA) / I_{100} Anatase for 30TiO_2-BEA progressively varies in this sense, as 5.1 for the undoped sample. This ratio decreases more slowly from 1.2, 1.0, and 0.9, indicating the progressive crystal growth of anatase induced by the previous Ag-doping. This improved crystallization allowed that (004), (200), (105), and (211) peaks of the anatase phase can also be clearly identified. These results are in agreement with those based on textural transformations, larger anatase particles are formed offside mesopores, in such a way that the TiO_2 crystallite size increased from 12 (without Ag) to 18 nm for 30TiO_2–5Ag-BEA. When comparing the XRD patterns of samples prepared by IE or IWI, doped in both cases with 3.5 wt% of Ag, clearly the ratio I_{100} (BEA) / I_{100} anatase phase is higher in the case of doping by IWI, denoting either a smaller crystallinity or a smaller particle size, regarding TiO_2. In fact, the crystal size of anatase in the IWI-doped composite does not change significantly regarding 30TiO_2-BEA (i.e., around 12 nm), because this phase was synthesized before doping.

In contrast to the exposed effect exerted for exchanged Ag-species on the BEA surface, favoring the TiO_2 crystal growth, Al Amin et al. [29] found that the incorporation of Ag^+ ions into the TiO_2 structure, namely on the grain boundaries, restricted grain coarsening and growth when preparing films of TiO_2 or TiO_2-Ag by a sol-gel procedure using a Ti-alkoxide in ethanol and $AgNO_3$ as dopant agent. Similarly, Liza et al. [20] described that the XRD peaks of anatase progressively shifted to lower 2θ values with increasing concentration of Ag-doping. The incorporation of Ag^+ into the anatase structure produces a charge unbalance that is compensated with the generation of oxygen vacancies. Shi et al. [30] also describes the incorporation of Ag^+ into the anatase structure of hollow TiO_2 nanoparticles and the XRD peak displacement to lower angles. The grain aggregation (sintering) and the anatase-rutile transformation during high-temperature calcination can be effectively retarded by controlling the Ag-loading.

Thus, in general, it is assumed that Ag-doping induces a smaller crystal size and the formation of imperfections, pointed out by changes in the profile and position of the XRD peaks, as commented. However, in our case, sharper peaks are obtained with increasing IE Ag-loadings (Fig. 3), together with a progressive shift of XRD peaks to higher values of 2θ. Nevertheless, whereas doping in previous studies is performed on precursor mixtures during sol-gel synthesis, in our case, the Ag species introduced by ion exchange (IE) on BEA are strongly anchored to the zeolite framework. This results in limited mobility, which restricts the incorporation of Ag^+ into the anatase structure. Consequently, a more homogeneous and orderly anatase crystal growth is promoted, further facilitated by the fact that crystallization occurs within a more open porosity (external surface). Even if compared with the doped IWI sample (Fig. S4), where, as commented, the anatase crystals were already formed before doping, the displacement to higher 2θ values is greater on the IE samples, denoting the strong effect of exchanged cationic Ag^+ enhancing the anatase crystal growth free of imperfections regarding the IWI-doped sample.

To complement the XRD conclusions and confirm the nature of interactions, the composites were analyzed by XPS. Table 2 summarizes the surface compositions of materials containing 30 wt% of TiO_2, including those prepared without Ag, compared to those doped with Ag by IE or IWI. The deconvolution and integration of the different spectral regions allow the quantification of the surface composition of materials, listed in Table 2, while the nature and distribution of both Ti and Ag chemical species, binding energies (BE), and percentages are summarized in Table 3.

The detection of Si/Al in all samples denotes that the zeolite surface is never totally covered by the TiO_2 phase, regardless of this phase being directly deposited on the H-BEA or IE Ag-BEA zeolite. The oxygen content on the surface decreases in all the Ag-doped composites regarding the undoped one, being, however, very similar between them. Nevertheless, it is noteworthy that in the IE series the Si content increased regarding 30TiO_2-BEA, while the Ti content decreased in a similar proportion. These changes in the Si/Ti surface composition are evidently smaller in the case of the IWI sample. Since the TiO_2 loading is fixed in all cases at 30 wt%, these variations are due to the different crystal size and localization of the anatase phase into the zeolite porosity. Sintering and localization of anatase or Ag nanoparticles inside

Table 2
Atomic surface content of the different materials determined by XPS.

Sample	O (%)	Si (%)	Ti (%)	Ag (%)	Al (%)	N (%)
30TiO_2-BEA	70.6	10.7	16.1	–	1.1	1.6
30TiO_2–1.0Ag-BEA	67.8	20.0	8.7	1.0	1.7	0.8
30TiO_2–3.5Ag-BEA	68.0	19.2	8.5	1.7	1.7	0.9
30TiO_2–5.0Ag-BEA	65.5	16.7	13.2	2.2	1.6	0.8
30TiO_2-BEA-3.5Ag	66.7	12.2	17.4	1.3	1.6	0.8

Table 3
- Distribution of chemical species on the catalysts surface determined by XPS.

Sample	Ti 2p				Ag 3d			
	Ti^{4+} $2p_{3/2}$	%	$Ti^{+4+\phi}$ $2p_{3/2}$	%	Ag^{0} $3d_{5/2}$	%	Ag^{+} $3d_{5/2}$	%
$30TiO_2$-BEA	458.7	100	–	–	–	–	–	–
$30TiO_2$–1.0Ag-BEA	458.6	67	460.2	33	–	–	368.7	100
$30TiO_2$–3.5Ag-BEA	458.5	57	459.7	43	–	–	368.7	100
$30TiO_2$–5.0Ag-BEA	458.5	71	459.9	30	367.4	42	368.7	58
$30TiO_2$-BEA-3.5Ag	458.5	100	–	–	368.0	100	–	–

the porosity should cause their respective contents to decrease, as XPS analysis has a limited depth. As mentioned in the previous paragraphs, increasing the Ag loading via ion exchange (IE) leads to the formation of TiO_2 crystals within progressively larger pores, i.e., on increasingly external surfaces, which should enhance the detectability of anatase (Ti) as the Ag content increases. This fact could justify the higher Ti-surface content in the sample doped at 5 wt% Ag despite the great particle size demonstrated by XRD and HRTEM in this case.

Regarding the Ag-content detected by XPS, in the case of IE samples, it linearly increased with the metal loading, although this increase is proportionally smaller regarding the theoretical Ag loadings (i.e., 2.2 vs 5.0). Comparing IE samples with sample IWI, a greater Ag content was expected in the latter, because in this case, doping with Ag was the last step of preparation, and the impregnation technique also favors the formation of nanoparticles on the external surface. Nevertheless, the Ag content detected by XPS is smaller for the sample $30TiO_2$-BEA-3.5Ag than for $30TiO_2$–3.5Ag-BEA. The results are again strongly influenced by the Ag dispersion.

XPS, however, provides interesting results regarding the different chemical characteristics and, therefore, different interactions between phases in each case. For that, the different spectral regions were treated carefully. Changes in the Ti and Ag species were identified and quantified by analyzing the Ti 2p and Ag 3d spectral regions, but also, the analysis of the O1s showed interesting results about the bond nature and functionalization of surfaces.

When TiO_2 is supported on zeolite H-BEA (sample $30TiO_2$-BEA), the Ti 2p profile (Fig. 4a) shows a doublet at 458.6 eV- 464.2 eV, denoting Ti^{4+} as the unique Ti-specie observed [31]. However, when the BEA

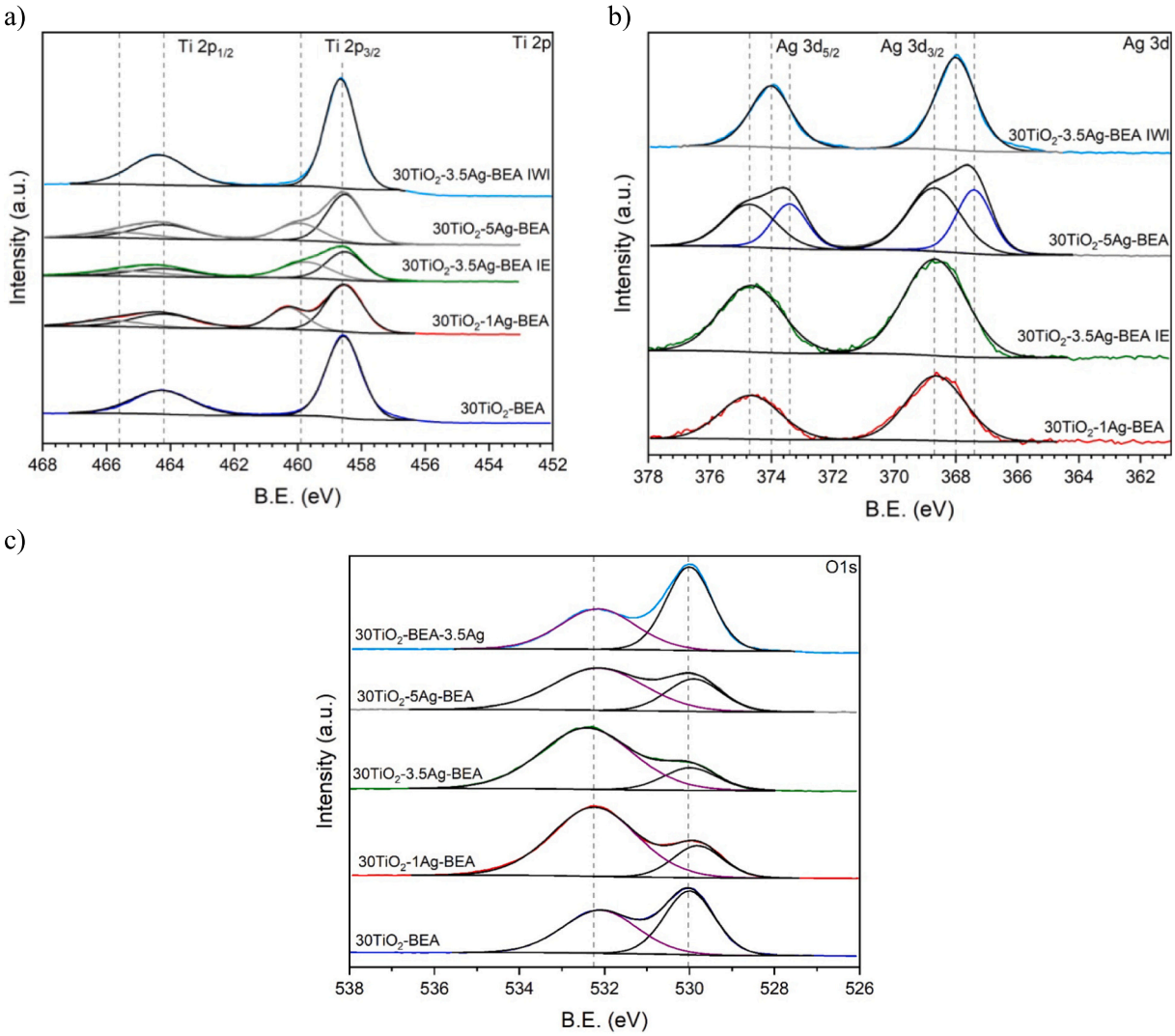

Fig. 4. XPS spectra of the Ag-based composites and the composite without Ag in the regions a) Ti 2p, b) Ag 3d, and c) O1s.

zeolite is previously exchanged with Ag (composites IE), the profile of the Ti 2p spectral region is split into two components, with a new component showing a doublet at 459.9–465.6 eV. The BE displacement to higher values indicates a poorer electronic environment of the new Ti-phase. Nevertheless, this effect is not observed when the Ag doping is carried out by IWI (sample 30TiO_2-BEA-3.5Ag). In fact, the BE of the Ti^{+4} species slowly decreases (around 0.2 eV) regarding the undoped sample (Table 3).

When analyzing the Ag 3d spectral region (Fig. 4b), it is observed that the Ag species exhibit just the opposite behavior. When doping by IE, only the peaks corresponding to Ag^+ species at 368.7–374.7 eV are observed for the composites doped at 1 and 3.5 % Ag. Contrarily, in the case of the composite doped by IWI at 3.5 %-Ag, only Ag^0 is detected. The analysis of this spectral region for the sample IE doped with 5 % Ag pointed out that a second Ag phase is clearly formed. In this case, the splitting of the Ag-profile generated a new component at lower BE, a new doublet appears at 367.4–373.4 eV, which is assigned to metallic Ag^0 according to literature values [32].

These results are in agreement with those previously described about the segregation of extra-framework Ag nanoparticles as the Ag loading increases. Ionic Ag^+ exchanged into the zeolite framework remains as Ag^+. Extra framework silver species are forming nanoparticles progressively greater in a more external surface, which, considering the noble character of silver, and the well-known easy reduction of Ag^+ species by temperature, light, or solvents (ethanol) [33,34], are as Ag^0 in the final IE doped composites.

Therefore, results clearly confirm the electronic transfers between Ag and anatase phases, regulated by the chemical state of the Ag. When the anatase crystal grows on IE-exchanged zeolites, the Ag^+ species generates a strong electro-deficient environment, BE of Ti^{+4} tends to increase because the electronic interactions generate a new electron-depleted $Ti^{+4+\phi}$ state, as clearly observed in Fig. 4a. However, if the anatase was previously supported on the zeolite, the BE of Ti^{+4} species after doping with Ag by IWI is maintained or slightly tends to decrease. Shi et al. [30] also commented on the electron redistribution because Ag doping alters the original chemical state of TiO_2 during the sol-gel synthesis. They found that Ti 2p peaks shifted towards lower binding energy, resulting in a decrease of approximately 0.23 eV after doping with Ag at 0.2 wt% due to the introduction of Ag^+ into positions of Ti^{+4} in the anatase structure and the consequent compensation by generating oxygen vacancies.

In our case, when comparing the O 1 s spectral region of IE and IWI Ag-composites, significant differences are also observed (Fig. 4c). Although this region was fitted in both cases with only two components, at around 529.8 and 532.1 eV, the proportion of both types of oxygenated surface groups (OSG) dramatically changes. OSG with high BE is favored in the case of the IE composite. According to the bibliography, in pristine TiO_2, the peak at around 530 eV is assigned to Ti—O bonds, while a second one at around 531.4 eV corresponds to OH functionalities. Moreover, the contribution of Si—O and Al—O bonds from the zeolite structure should be considered. In fact, the increase in this peak is correlated to the increase in Si content visible at the surface. The position of this last peak changes in the presence of other functionalities, like N. Thus, the formation of Ti-O-N bonds, as an example, increased the BE up to 532.3 eV [35]. Although in our case the distribution of OSG should be influenced by the changes in the surface composition, the higher proportion of high BE OSG in the case of IE doped composites denotes that oxygen is linked to a more electron-deficient species, probably related to the detected $Ti^{+4+\phi}$.

When zeolite is treated in the $AgNO_3$ solutions, the ionic exchange of H^+ by Ag^+ competes with the precipitation of metallic species on the zeolite surface. Precipitation is clearly enhanced by increasing the concentration of the metal precursors, leading to the formation of progressively larger metallic particles on the surface. At low Ag-loadings, a large part of Ag^+ is fixed onto the zeolite structure by ion exchange, remaining as Ag^+, although the formation of Ag^0 nanoparticles was observed by HRTEM. However, this trend significantly changes in the sample with 5 wt% Ag, where precipitation and the Ag-nanoparticle size strongly increase. These extraframework nanoparticles are located on a more external surface, as demonstrated by analyzing the PSD, thus favoring the contact with radiation and TiO_2 phase, and consequently can be easily reduced, forming the metallic Ag^0 as identified by XPS. Cationic Ag^+ is primarily incorporated into the zeolite framework, clearly modifying the electrochemical behavior of the zeolite surface in comparison with the surface of raw H-BEA zeolite. After TiO_2 coating, exchanged Ag^+ species destabilize the anatase structure, and the concentration of the electron-depleted $Ti^{+4+\phi}$ increases. Increasing Ag loading, a greater proportion of $Ti^{+4+\phi}$ is detected while Ag species are reduced to Ag^0 in a concentration that becomes suitable to be detected.

These conclusions are further supported by H_2-TPR analysis (Fig. 5). The TPR profiles of the Ag-based composites show a prominent and sharp peak, with a distinct shoulder. Changes in the profile and position of the peaks clearly indicate the presence of different Ag species depending on the Ag-loading and preparation procedure. Monovalent Ag^+ species, stabilized in the zeolites, normally exhibit two reduction peaks: one at lower temperatures (90–150 °C) corresponding to the reduction of Ag^+ to Ag_4^{2+}, and a second at higher temperatures (200–500 °C) attributed to the reduction of Ag_4^{2+} to Ag^0 [36,37].

The three IE Ag-based materials display two overlapping reduction peaks. The peak maxima are observed at 185 °C, 150 °C, and 125 °C for the composites containing 1, 3.5, and 5 wt% of Ag, respectively. Thus, reduction became progressively easier with increasing metal loading because, in this sense, large particles are formed, allowing the reduction mechanism exposed before. This reduction temperature range is characteristic of Ag^+ (usually in the form of Ag_2O) and cationic $Ag_n^{\delta+}$ clusters. The 30TiO_2–1.0Ag-BEA composite shows a higher reduction temperature compared to the other composite, confirming a strong interaction between the Ag^+ species and the zeolite framework. The small shoulder at low temperature corresponds to the formation of small $Ag_n^{\delta+}$ clusters and Ag_2O nanoparticles. As the Ag content increases, the reduction peak broadens, and its maximum shifts to lower temperatures. This behavior confirms that the increase in Ag content facilitates the formation of larger extra-framework particles, with weaker contact with the zeolite structure and consequently more easily reduced than the smaller ones. It is also remarkable the change in the profile. As commented, at 1 % Ag, a small shoulder appears at a lower temperature. With increasing Ag loading, the shoulder appears at a higher temperature, which agrees with the increase of nanoparticle size denoted by HRTEM or DRX, as well, the progressive reduction of these nanoparticles, as denoted by

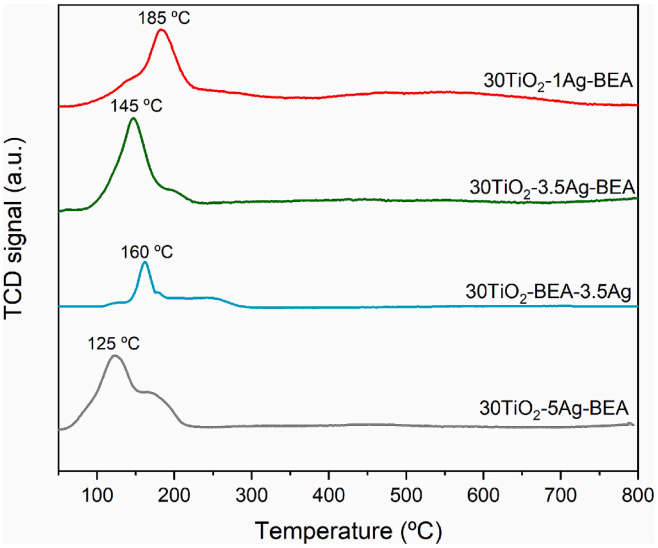

Fig. 5. H_2-TPR profiles for Ag-based composites.

XPS. Nevertheless, despite the clear weakening of interactions, at 3.5 % Ag, there is a significant fraction of Ag species reduced at 185 °C, and at 5 % a large shoulder is observed at around 160 °C. With increasing Ag loading, the increasing proportion of auto-reduced Ag^0 species causes the area involved by these curves (H_2 consumption) to not increase linearly with the Ag loadings.

The TPR signal is especially weak when analyzing the 30TiO_2-BEA-3.5Ag (IWI). Although it was noted by XPS that only Ag^0 appears on the surface, TPR results confirm that a certain fraction of Ag is oxidized. Large particles on the external surface correspond, therefore, mainly to Ag^0. However, the Si and Al contents detected also by XPS corroborated that the zeolite surface was not totally covered with the TiO_2 phase. Thus, there is also a small fraction of Ag-species located on the zeolite framework (not detected by XPS), which can be stabilized as clusters of $Ag_n^{\delta+}$ or even form small Ag_2O nanoparticles. In any case, these species contributed to the H_2 consumption during TPR of the IWI composite. This fraction of the Ag-loading is strongly anchored to the zeolite framework, TPR peaks being observed at temperatures significantly higher than in the corresponding IE composite.

The smaller TiO_2 crystal size, as the formation of TiO_2-Ag heterojunction was expected to exert some effect on the visible light absorption of TiO_2, because the energetic levels are modified by both factors [20,29,30]. The number of overlapping orbitals or energy levels increases as small as the particle size is, while doping with transition metals (Ag) generates new electronic states in the band gap. As an example, Liza et al. [20] found that the BG of undoped TiO_2 is 3.29 eV, which decreased to 2.94 and 2.73 eV after doping with 2.5 % and 3 % Ag, respectively, because the absorption spectrum shifted towards the higher wavelength region, an effect called “Red Shift”.

The UV–Vis DRS spectra of our composites prepared by different doping procedures are shown in Fig. 6a. Although the spectra clearly resemble the behavior of pure TiO_2 phase with a strong radiation absorption at $\lambda < 400$ nm, the composite 30TiO_2-BEA-3.5Ag showed a greater interaction with the radiation than their homologous 30TiO_2–3.5Ag-BEA, and in this sense, there is a slow decrease in the BG values calculated from the corresponding Tauc plots (Fig. 6b). This best performance seems to be related to the smaller anatase crystal (around 12 nm) and the formation of effective TiO_2/Ag heterojunctions. In the composite prepared by IE, the main fraction of the silver remains as Ag_2O, being strongly linked to the zeolite framework; only the extraframework nanoparticles of Ag^0 are also suitable for the formation of the heterojunction. In fact, in the IE series, the BG value also slowly decreases with increasing Ag-loadings (see Table S2 and Fig. S5), because, in this sense, it also increases the extraframework Ag^0 nanoparticles. Nevertheless, with increasing Ag-loading, the anatase crystal size also increases from 12 to 21 nm. Thus, although it was expected that the plasmonic effect of Ag-nanoparticles improved the absorption at higher wavenumber, this effect is very weak even in the best case, thus causing a scarce effect on the BG value, probably due to a compensation of effects with the anatase crystal growth.

3.2. About ethylene removal

The ability of the samples to remove ethylene from the flow is analyzed below using two different approaches: adsorption and catalysis. In the first case, as this is not a destructive technique, the ethylene could be stored in this way until the fruit is ready to be sold and controlled ripening is required. Catalysis, on the other hand, attempts to transform it into products that do not interfere with the ripening of the fruit. Establishing the role of each of the component (the zeolite as a support for the active phase (TiO_2) and Ag as doping agent) in both processes, based on the physicochemical characterization presented above, is key to monitoring the information derived from each section.

It should also be noted that the photocatalytic tests were carried out after saturating the samples in darkness. This conditions the analysis of results, the handling of which we therefore wish to define in advance. Since the elimination of ethylene (in conversion values) can be affected by adsorption, and for the purposes of comparison between samples or under different experimental conditions, the monitoring of the reaction is discussed simultaneously on the basis of product formation. On the other hand, the pre-adsorption of ethylene generates a high concentration of ethylene on the surface, so that in the transition between adsorption and catalysis, the activation of the surface causes the simultaneous desorption and oxidation of the adsorbed species, generating negative ethylene conversion values and very high CO2 generation values during this period. All these aspects are discussed in detail below.

3.2.1. Adsorption - pretreatment

Before each photooxidation reaction, ethylene was passed through the materials in the dark until saturation, in order to avoid the contribution of adsorption when determining the ethylene removal by oxidation. The total amount of ethylene adsorbed was calculated (Fig. 7) from the corresponding breakthrough curves (Fig. S6) recorded. All the adsorption curves presented here were obtained under the following conditions: 100 ppm of ethylene, 21 % O_2, no humidity (dry air), and a total flow of 25 ml.min^{-1}. Ethylene adsorption on raw BEA zeolite is

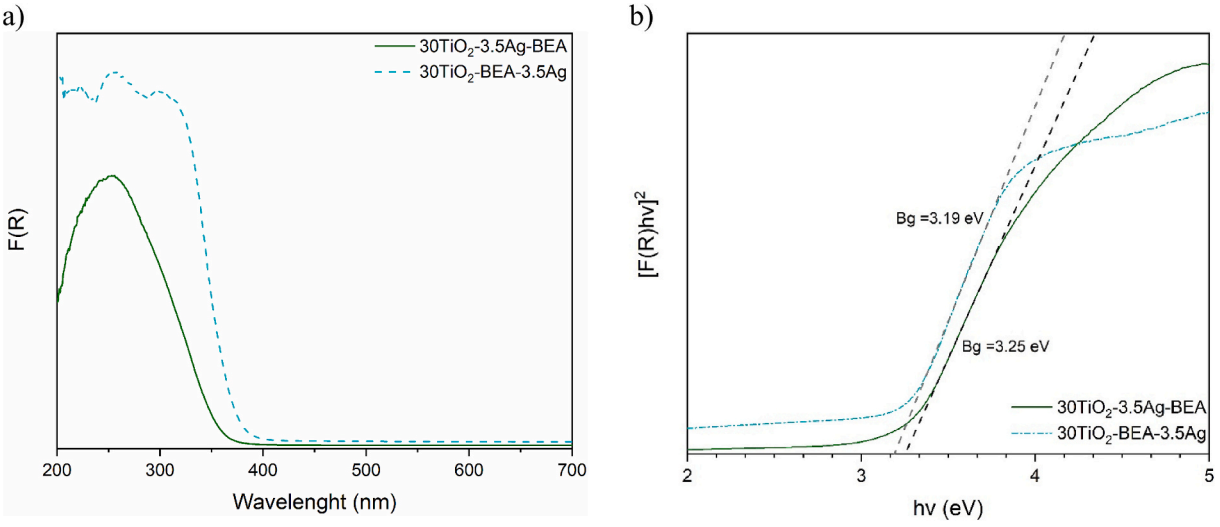

Fig. 6. Comparison of the light absorption of composites doped by different methods. A) UV–Vis DRS spectra and b) Tauc plots of samples 30TiO_2–3.5Ag-BEA (—) and 30TiO_2-BEA-3.5Ag (—·—).

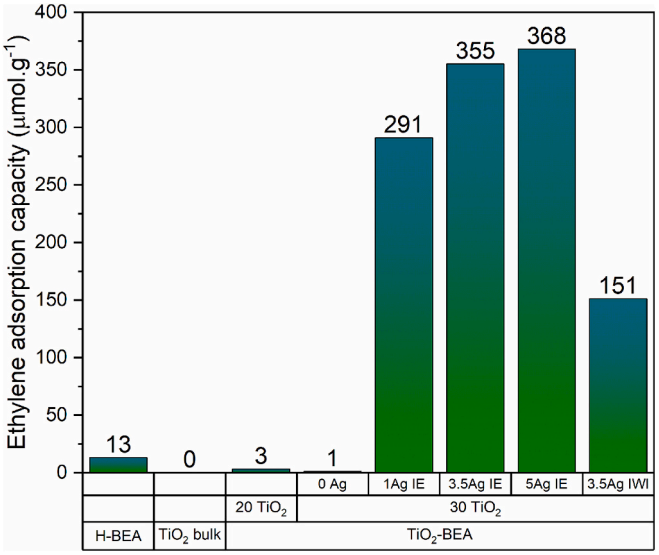

Fig. 7. Ethylene adsorption capacity from parent zeolite, TiO_2 bulk, composites without Ag, and Ag-based composites, under 0.45 g of catalyst, 21 % O_2, 0 % RH, 100 ppm C_2H_4.

rather small, but negligible on the TiO_2 bulk sample. Thus, this parameter is also significantly constrained in the TiO_2-BEA composites, exhibiting only a slight decrease as a function of TiO_2 loading. The adsorption capacity significantly increases in the TiO_2-Ag-BEA composites (Fig. 7). Ethylene adsorption is favored mainly on Ag^+ species [14]. However, Ag_2O and $Ag_n^{\delta+}$ clusters can also interact with ethylene [16,17]. Fig. S6b presents the ethylene breakthrough curves for the Ag-based composites, which show the longer breakthrough or saturation times for these samples, leading to a substantial increase in the amount of ethylene adsorbed (from 1 to 291 μmol.g^{-1}, for samples 30TiO_2-BEA and 30TiO_2–1Ag-BEA, respectively). Taking into account that Ag-exchanged samples present smaller S_{BET} or S_{ext} values (Table 1), these results confirm that the Ag species present in the composite are responsible for the strong interaction with ethylene [14,16,17] and the subsequent improved adsorption capacity. Increasing the amount of Ag, ethylene adsorption also increases. Nevertheless, despite the strong adsorption increase produced after doping only with 1 wt% regarding the undoped composite, the improvement of the adsorption capacity is significantly smaller for greater Ag loadings. Thus, when Ag loading increases 5 times, the adsorption capacity only increases 27 % (from 291 to 368 μmol·g^{-1}), clearly related to the progressive sintering and the deposition of Ag^0, which are not involved in the adsorption processes. As expected from sample 30TiO_2-BEA-3.5Ag, the adsorption capacity of this sample is much lower than the remaining samples. Even so, the ethylene adsorption capacity here from this sample is significantly higher than the undoped samples, meaning that the low concentration of Ag^+ species observed by TPR (Fig. 5) is, in fact, contributing to increasing the ethylene adsorption capacity.

The adsorption of ethylene is quite limited in most adsorbents because the non-polar nature of this molecule avoids electrostatic interactions. This limits the possibility of using inorganic adsorbents or improving adsorption by modifying their surface chemistry, since surface groups are generally polar. The ethylene adsorption bibliography is also limited, probably due to the same issue, and focuses on analyzing other aspects, such as the separation of ethylene/ethane mixtures. Furthermore, it is still more difficult to make comparisons with our results, considering that we analyze the performance of samples under dynamic adsorption conditions, whereas most studies estimate adsorption capacity under static conditions.

As shown in Fig. 7, ethylene adsorption on TiO_2 is negligible, suggesting the necessity of combining it with porous supports. Nevertheless, even the adsorption capacity of highly porous BEA is quite limited (13 μmol g^{-1}). These results are consistent with those obtained by other authors using different zeolites. Cisneros et al. [38] demonstrated that ethylene adsorption on zeolites can be enhanced through doping with Ag. The zeolite framework stabilizes the Ag^+ species responsible for ethylene adsorption via π-complexation. Based on this, Monzón et al. [39] found that the adsorption capacity of zeolite A modified with Ag by ionic exchange reached an ethylene adsorption capacity of around 2.5 mol.kg^{-1} of adsorbent in the best case, as determined in static conditions using a Micromeritics ASAP 2020 instrument. These results are a function of the chemical nature of the Ag species and their accessibility into the porous system (thermal treatment).

Very recently, Pereyra et al. [40] developed a series of zeolite A samples exchanged with Na^+, Ag^+ or Zn^{+2} and their combinations for use in active fruit packaging. The best results under static conditions were in the same range as those detected by Monzón, i.e., 2402 μmol.g^{-1} at $P/P_o = 1$ when exchanged with Ag at 40 wt%. The authors propose two adsorption mechanisms: in samples exchanged with alkali (Na^+, K^+) or alkali-earth (Ca^{+2}) cations a reversible but weak interaction with the oxygen of the framework occurs, while covalent π-complexation occurs with transition metals via a dπ-pπ* back-bonding interaction. For comparison, note that we are working in flow at a low P/P_o, approximately $P/P_o = 0.08$ (100 ppm). According to the isotherms provided by Pereyra, even for Ag-exchanged zeolite, the amount adsorbed in equilibrium at this P/P_o value is around 240 μmol.g^{-1} (1/10 of the total adsorption capacity). This demonstrates the good performance of our samples, considering that we reach around 370 μmol.g^{-1} in dynamic conditions with an Ag loading of 5 wt%.

Carbon materials are also an interesting, porous alternative for ethylene adsorption. Regadera et al. [27] developed activated carbons (ACs) for ethylene removal by adsorption. These carbon materials can interact with ethylene via π-π interactions between the adsorbents' aromatic structures and the ethylene molecule's double bond. Depending on the synthesis procedure for metal-free ACs, the adsorption capacity for 100 ppm of ethylene in dynamic conditions varies between 116 and 181 μmol.g^{-1}. It has been suggested that using carbon materials as ethylene adsorbents can have a negative effect when heteroatoms are introduced [41], while removing oxygenated surface groups by reduction in H_2 can greatly enhance ethylene adsorption on sp^2 surfaces, achieving values of around 2500 μmol.g^{-1}, which are comparable to those obtained with Ag-exchanged zeolites [42].

3.2.2. *Ethylene photooxidation*

3.2.2.1. Effect of the type of radiation. From an economic and environmental perspective, it is more desirable for photocatalytic reactions to be performed under natural solar radiation. To address this, we conducted a study to evaluate the catalytic behavior of the composites under UV–Vis and UVA-Vis radiation spectra. The performance of pure phases, BEA zeolite and TiO_2 bulk, as well as their composites 20TiO_2-BEA and 30TiO_2-BEA, were analyzed under both radiations (Fig. 8) while maintaining the rest of the experimental conditions (flow rate and concentrations) used in the adsorption tests in the dark. BEA zeolite demonstrated no photocatalytic activity. Under UV radiation, both bulk and composite materials completely remove the ethylene in the flow (Fig. 8a). When using less energetic radiation (UVA-Vis, Fig. 8b), the catalytic performance decreases, allowing differentiation between samples. Despite the high activity of composite 20TiO_2-BEA, in these conditions, total conversion is achieved only using bulk TiO_2 or 30TiO_2-BEA. These results clearly demonstrate the advantage of supported catalysts regarding the bulk phase. Photocatalysts with a TiO_2 loading between 20 and 30 wt% also reach total conversion of ethylene. Only CO_2 was detected as reaction product, and the carbon um-balance smaller than 2 % in any case, either under UV or Vis-radiation, thus, even under this less energetic radiation, the photooxidation proceeded

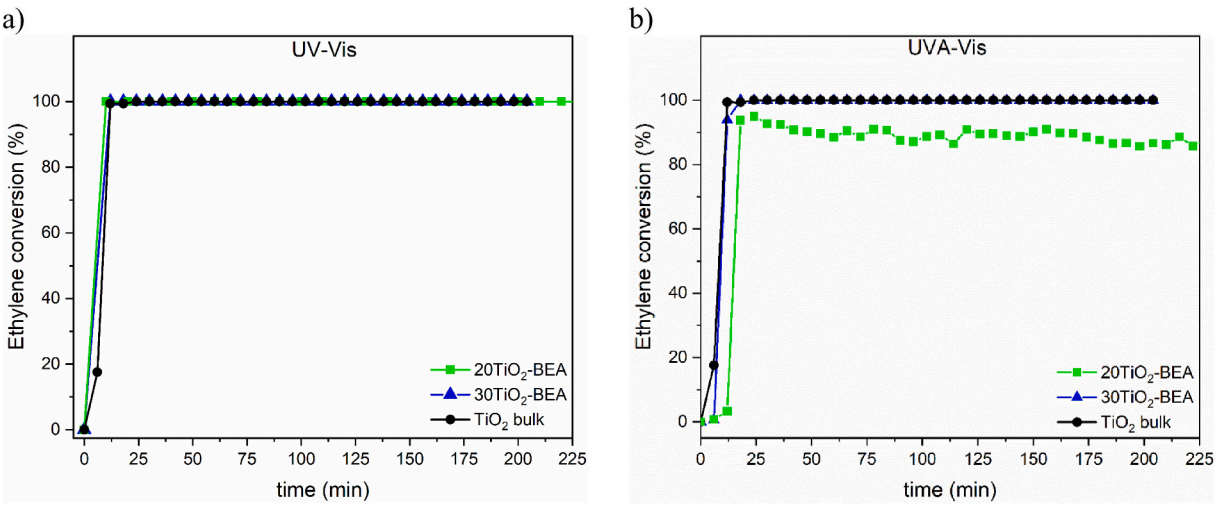

Fig. 8. Ethylene photooxidation conversion over time in a) UV–Vis irradiation and b) UVA-Vis irradiation for composites $20TiO_2$-BEA (■), $30TiO_2$-BEA (▲), and TiO_2 bulk (●), under 0.45 g of catalyst, 21 % O_2, 0 % RH, 100 ppm C_2H_4.

selectively to CO_2. Based on these results, the formation of CO_2 will be presented along the manuscript mainly as TOF to facilitate the comparison between samples with different TiO_2 loadings, and sample $20TiO_2$-BEA was selected to analyze the influence of different experimental conditions under UVA-Vis radiation.

3.3. Effect of the concentration of C_2H_4

Several authors have demonstrated that ethylene photooxidation follows Langmuir−Hinshelwood kinetics [43], where conversion typically increases with increasing initial concentration. We used two ethylene concentrations (100 and 200 ppm) to study the influence of this parameter. Fig. 9 presents the activity of the samples in terms of ethylene conversion and turnover frequency (TOF) for CO_2 production. In terms of ethylene removal, the experiment with 200 ppm of ethylene achieved approximately half the conversion observed with 100 ppm (around 90 %, as determined previously). However, when examining the TOF values for the CO_2 formation, both curves (100 and 200 ppm) appear very similar, nearly overlapping each other. This observation confirms that the active sites of the composite are almost fully utilized at 100 ppm of ethylene, and no additional ethylene molecules can be transformed by unit of time, maintaining the conditions of radiation, room temperature, and pressure.

3.4. Effect of the presence of water

Due to the importance of humidity in the atmosphere of fruit storage cameras, the influence of water presence was investigated by analyzing the performance of $20TiO_2$-BEA composite under a dry flow (relative humidity, RH = 0 %) compared to a flow with RH adjusted to 50 %. The results obtained maintaining flow, concentrations, and UVA-Vis radiation are presented in Fig. 10. It can be observed that ethylene conversion decreases significantly, from around 90 % under dry conditions to 35 % in the presence of humidity in the flow (Fig. 10). Under dry conditions, ethylene removal quickly reaches high conversion values, followed by a gradual decrease around a steady mean value. Similarly, the CO_2 formation (represented as TOF) initially increases but soon stabilizes, reaching a stationary state.

Under wet conditions (50 % RH), the formation of highly reactive $HO^{\bullet}$ radicals should enhance the photocatalytic process. However, the percentage of ethylene removal is initially very low in these experimental conditions, and although it gradually increases over time, the ethylene conversion remains approximately only around 35 % in the stationary state. In contrast, at the beginning of the reaction, CO_2

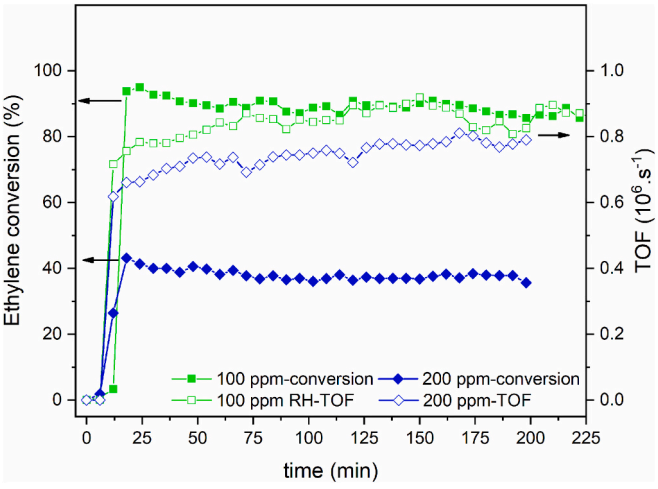

Fig. 9. Ethylene conversion and TOF over time of sample $20TiO_2$-BEA with 100 (■) and 200 (◆) ppm of C_2H_4, under UVA-Vis, 0.45 g of catalyst, 21 % O_2, and 100 ppm C_2H_4.

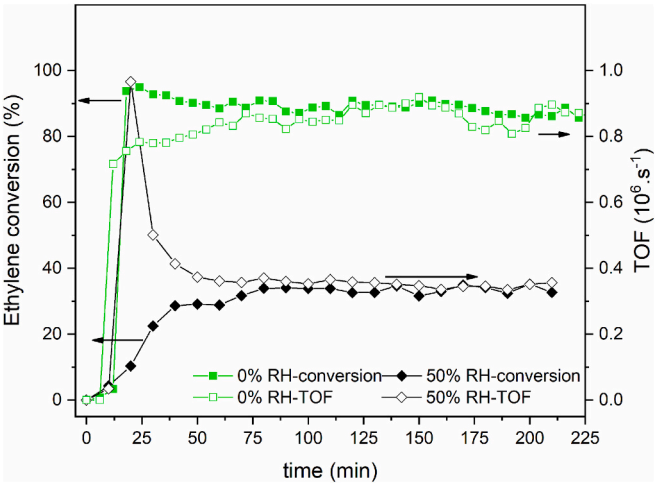

Fig. 10. Ethylene conversion and TOF over time of sample $20TiO_2$-BEA with 0 (■) and 50 (◆) % RH, under UVA-Vis, 0.45 g of catalyst, 21 % O_2, 100 ppm C_2H_4.

formation showed a pronounced maximum at short reaction times. The low ethylene conversion is attributed to competitive adsorption between water and ethylene molecules, water adsorption favored by the hydrophilic nature of the zeolite support [44]. The observed CO_2 peak indicates that ethylene adsorbed during the pretreatment step (see Fig. S7) (dark) is rapidly displaced by water and subsequently oxidized under radiation.

The overall yield depends on the entire reaction mechanism, with water adsorption potentially inhibiting the already limited ethylene adsorption on inorganic composites, given the nonpolar nature of the ethylene molecule. Hussain et al. [45] demonstrated that water competes with ethylene for the same adsorption sites, thereby reducing the contact between ethylene and the photocatalyst. Zhang et al. [46] further showed that while an increase in water content benefits the photooxidation of long-chain carbon molecules, for shorter-chain carbon molecules, lower water concentrations may be more impactful.

3.5. Effect of the concentration of O_2

Under dry conditions, the oxidant radical species (i.e., superoxide anion, $O_2^{\bullet-}$) are generated by reduction of O_2 by the photo-excited electrons of the CB of TiO_2. It has been suggested that O_2 is a better source of radicals for photooxidation due to its longer lifetime [47]. Thus, to investigate the influence of this parameter, two O_2 concentrations were used. Fig. 11 compares the catalytic behavior obtained when the O_2 concentration was varied. Decreasing O_2 concentration from 21 to 16 %, ethylene conversion decreases from 90 to 30 % with TOF values changing in a similar proportion. This confirms that dry photooxidation proceeds via $O_2^{\bullet-}$ radicals, which are significantly limited when the O_2 concentration is reduced (photo-oxidation is reduced to a greater extent than the O_2 concentration).

3.6. Effect of Ag-doping

The positive influence of Ag species on the ethylene adsorption capacity of samples was previously commented. On this basis, it was expected that the higher adsorption capacity of the Ag-BEA support could improve the overall performance of their derivative TiO_2 composites [4]. Fig. 12a shows the TOF regarding CO_2 production. Ethylene photooxidation follows a pattern similar to that of ethylene removal. Once the lamp was connected, both the ethylene desorption and the photooxidation to CO_2 are favored. At the beginning of the reaction, therefore, there is a strong formation of CO_2 by partially burning the pre-adsorbed ethylene. Then, the TOF values progressively decay until the catalysts reach the stationary state. In the experimental conditions used, 100 % of ethylene removal with a 100 % selectivity to CO_2 is always achieved after reaching the stationary state in all cases.

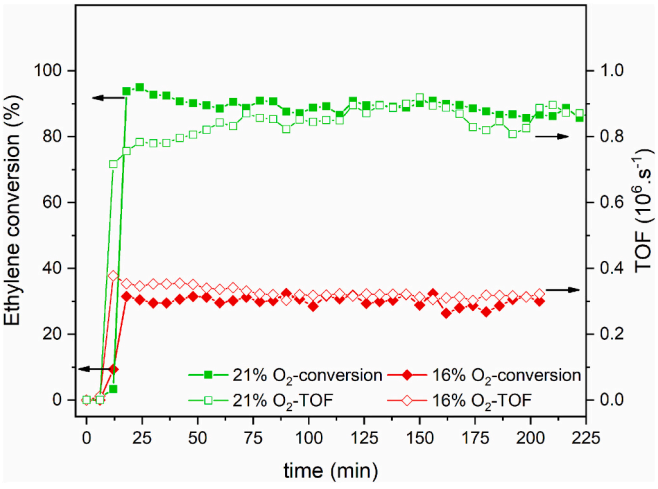

Fig. 11. Ethylene conversion and TOF over time of sample 20TiO_2-BEA with 16 (◆) and 21 (■) % O_2, under UVA-Vis, 0.45 g of catalyst, 0 % RH, 100 ppm C_2H_4.

Using 30TiO_2-BEA composite, the total ethylene combustion is achieved (Fig. 8), but the amount of pre-adsorbed ethylene is low (Fig. 7). Thus, the stationary state is quickly reached. Using IE TiO_2-Ag-BEA composites, the intensity of the initial peak, as well as the tail of the curve, progressively increased with the Ag loadings. Thus, the amount of ethylene oxidized in this period is favored because of the increase of pre-adsorbed ethylene, showing the benefits of doping with Ag.

It is noteworthy, however, that the formation of CO_2 is higher on the IWI-doped composite than the IE counterpart, or even higher than the sample doped at 5 %Ag by IE, despite the lower adsorption capacity of the IWI sample. These results confirm the importance of the chemical state and distribution of Ag-species. Ag^+ favors ethylene adsorption, while catalytic activity is favored by the formation of TiO_2/Ag^0 heterojunctions. In IE Ag-doped samples, increasing Ag loading increases the adsorption capacity, but also the formation of extra-framework Ag^0 nanoparticles. In IWI samples, the formation of active heterojunctions is comparatively enhanced. Nevertheless, both series of samples show a double adsorbent/photocatalytic capacity, because both functionalization (Ag^+/Ag^0) are present in both sample series, IE, favoring adsorption regarding the stronger catalytic performance of IWI samples. Anyway, the cumulative amount of CO_2 formed (Fig. 12b) progressively enhanced from bulk TiO_2 to supported photocatalysts and finally after doping with Ag. Thus, the positive effects of dispersing the semiconductor on the porous support, and mainly, Ag-doping and more specifically after formation of effective heterojunctions by IWI, are clearly demonstrated.

4. Conclusions

A series of photocatalysts based on TiO_2 were prepared by sol-gel techniques, and different actions were programmed to solve the classical drawback of TiO_2 photocatalysts, as low efficiency under solar radiation or high rates of recombination of photo-generated h^+/e^- pairs. The characteristics and performance of composites were tentatively optimized using BEA zeolite as support and fitting TiO_2 loadings. Further improvements were attempted by doping with Ag species. For that, two different approaches were also used: ionic exchange of the support before TiO_2 deposition or incipient wet impregnation of TiO_2-BEA composites.

Results obtained can be summarized as:

- The use of porous BEA zeolite allows for the production of highly dispersed nanocrystals of anatase, reducing the crystal size (recombination) up to TiO_2 loadings of around 20 wt% and slightly improving the ethylene adsorption capacity.
- In Ag-BEA prepared by IE, Ag^+ species are mainly fixed into the microporous structure of the zeolite, mainly remaining as Ag^+, although extra-framework Ag^0 nanoparticles are progressively formed as the Ag-loading increases. These processes indicate that during the posterior deposition of TiO_2, anatase nanocrystals should grow progressively in larger pores with highly electro-deficient surfaces. In consequence, with increasing concentration of Ag^+ exchanged, anatase crystals are progressively larger and electronic interactions generate TiO_2 phases electronically poorest ($Ti^{+4+\phi}$) while Ag-species are reduced to Ag^0. The strong nature of the established ionic bonds is pointed out by the predominance of oxygenated species with high B.E.
- When TiO_2 is deposited on the zeolite and then impregnated to generate the Ag-nanoparticles, the composites show a smaller anatase crystal size, especially at lower TiO_2 loadings. Only Ti^{+4} and Ag^0 species are identified, suggesting a correct formation of the TiO_2/Ag heterojunctions.
- Ethylene removal by adsorption is greatly improved in IE composites because the electronic configuration of Ag^+ species favors the

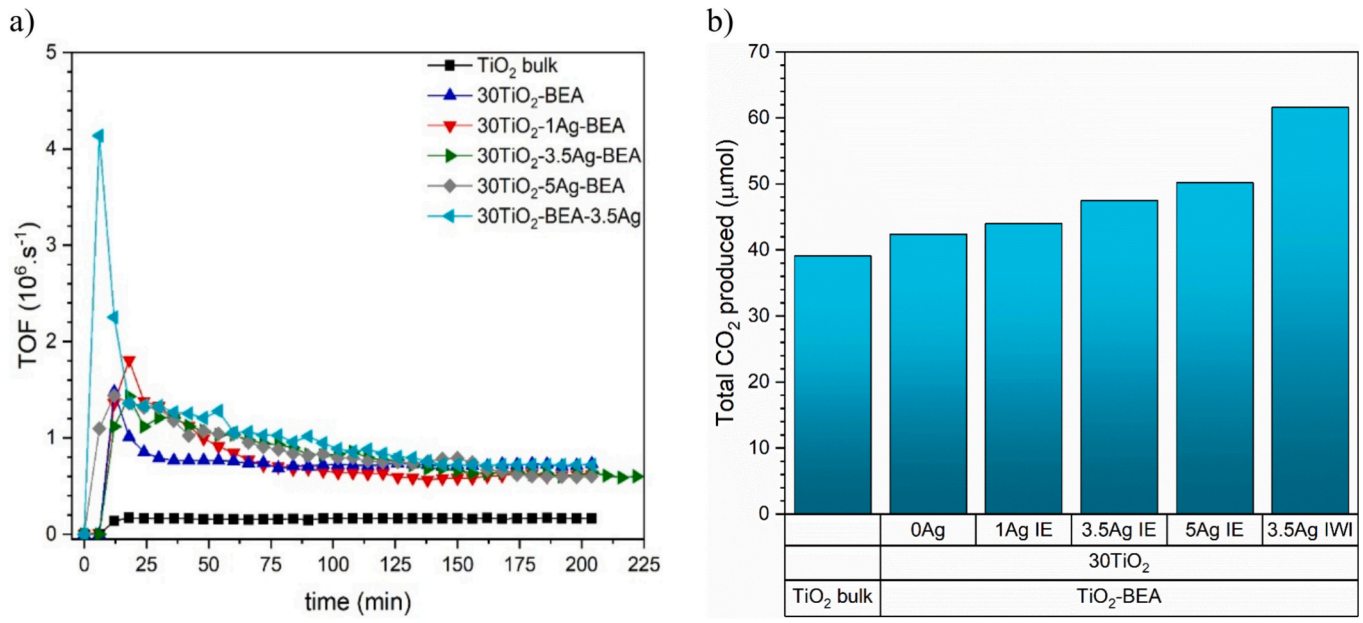

Fig. 12. a) TOF (regarding CO_2 yield), and b) CO_2 cumulative produced under 3 h and 30 mins by samples TiO_2 bulk (■), $30TiO_2$-BEA (▲), $30TiO_2$–1.0Ag-BEA (▼), $30TiO_2$–3.5Ag-BEA (►), $30TiO_2$-BEA-3.5Ag (◄), and $30TiO_2$–5Ag-BEA (◆), under UVA-Vis, 0.45 g of catalyst, 0 % RH, 21 % O_2, and 100 ppm C_2H_4.

complexation with the π-electrons of the ethylene molecule. Adsorption progressively improves with Ag-loading up to 5 wt%. The presence of humidity exerted a negative influence because there is competition with ethylene for the adsorption sites.

- Photocatalysts are active and totally selective for the total mineralization of ethylene to CO_2, even under visible radiation. However, the conversions strongly decreased again in the presence of humidity or oxygen concentration. The best catalytic performance is found by impregnation (IWI) of TiO_2-BEA composites, favored by a more preserved porosity and surface area values, smaller nanocrystals of anatase, and the formation of efficient TiO_2/Ag heterojunctions.
- In designing specific devices to be installed in large storage chambers of climacteric fruits, we can take advantage of the strong improvement of the ethylene adsorption capacity on Ag-exchanged zeolites and specific photocatalysts by doping via impregnation of deposited TiO_2 on the zeolite. A first column filled with Ag/zeolite can be used to pre-concentrate ethylene emitted by fruits by adsorption in the dark, followed by another column, or a section in the same column, containing the photocatalytic active phase highly dispersed on porous supports. After saturation of the first column, radiation is connected, favoring ethylene desorption in the first column and combustion in the second column, saving energy during the saturation periods. Alternatively, the use of independent columns can also permit the storage ethylene to be desorbed when the fruit will be commercialized, in order to provide the best quality to consumers.

CRediT authorship contribution statement

Ricardo Ferreira: Writing – original draft, Investigation. **Ana Regadera-Macías:** Investigation, Data curation. **Sergio Morales-Torres:** Writing – review & editing, Validation, Supervision, Formal analysis, Data curation. **Luisa M. Pastrana-Martínez:** Resources, Funding acquisition, Data curation. **João P. Lourenço:** Writing – original draft, Validation, Supervision, Methodology. **João M. Silva:** Writing – original draft, Resources, Data curation, Conceptualization. **Isabel M. João:** Visualization, Methodology, Data curation. **M. Filipa Ribeiro:** Writing – review & editing, Resources, Project administration, Methodology, Funding acquisition, Conceptualization. **Auguste Fernandes:** Writing – original draft, Supervision, Investigation, Data curation, Conceptualization. **Francisco J. Maldonado-Hódar:** Writing – review & editing, Writing – original draft, Project administration, Methodology, Funding acquisition, Data curation.

Declaration of competing interest

The authors declare that they have no known competing financial interests or personal relationships that could have appeared to influence the work reported in this paper.

Acknowledgments

The authors thank FCT for providing funding through projects Nano4fresh-PRIMA/0015/2019 (http://doi.org/10.54499/PRIMA/0015/2019), UIDP/00100/2020 (CQE) (doi:10.54499/UIDP/00100/2020), UID/00097/2030 (CEGIST) and LA/P/0056/2020 (IMS) (doi:10.54499/LA/P/0056/2020), project PCI2020-112045 from MCIN/AEI/10.13039/501100011033 and European Union Next Generation EU/PRTR; and by projects PID2021-126579OB-C31 funded through MCIN/AEI/10.13039/ 501100011033 and "ERDF A way of making Europe"; P21_00208 from Consejería de Universidad, Investigación e Innovación – Junta de Andalucía. SMT is grateful to MCIN/AEI/10.13039/501100011033 and the European Social Found (FSE) "El FSE invierte en tu futuro" for a Ramon y Cajal research contract (RYC-2019-026634-I). A. F. thanks Instituto Superior Técnico for the Scientific Employment contract under law DL 57/2016. R. Ferreira also thanks FCT for the PhD grant (2022.12593.BD). Funding for open access charge: Universidad de Granada / CBUA.

Appendix A. Supplementary data

Supplementary data to this article can be found online at https://doi.org/10.1016/j.seppur.2025.135302.

Data availability

No data was used for the research described in the article.

References

[1] M.H. Álvarez-Hernández, F. Artés-Hernández, F. Ávalos-Belmontes, M.A. Castillo-Campohermoso, J.C. Contreras-Esquivel, J.M. Ventura-Sobrevilla, G.B. Martínez-Hernández, Current scenario of adsorbent materials used in ethylene scavenging systems to extend fruit and vegetable postharvest life, Food Bioprocess Technol. 11 (2018) 511–525, https://doi.org/10.1007/s11947-018-2076-7.

[2] N. Pathak, P.V. Mahajan, Ethylene removal from fresh produce storage: Current methods and emerging technologies, in: Reference Module in Food Science, Elsevier, 2017, https://doi.org/10.1016/b978-0-08-100596-5.22330-5.

[3] M.A. Chiriboga, M. Saladié, J. Giné Bordonaba, I. Recasens, J. Garcia-Mas, C. Larrigaudière, Effect of cold storage and 1-MCP treatment on ethylene perception, signalling and synthesis: influence on the development of the evergreen behaviour in "conference" pears, Postharvest Biol. Technol. 86 (2013) 212–220, https://doi.org/10.1016/j.postharvbio.2013.07.003.

[4] N. Keller, M.N. Ducamp, D. Robert, V. Keller, Ethylene removal and fresh product storage: a challenge at the frontiers of chemistry. Toward an approach by photocatalytic oxidation, Chem. Rev. 113 (2013) 5029–5070, https://doi.org/10.1021/cr900398v.

[5] P.A. Nevado-Velasquez, J.G. Ramírez-Gil, C. García, D.A. Castellanos, A.A. Lopera, V.D. Nonato Bezzon, C. Paucar, Synthesis and application of ag-doped TiO2 nanoparticles with antifungal activity and ethylene inhibition in postharvest of avocado cv. Hass, Biocatal Agric, Biotechnol 54 (2023) 102901, https://doi.org/10.1016/j.bcab.2023.102901.

[6] D. Das, U.K. Panigrahi, J. Giri, A.K. Panda, P.K. Satapathy, P. Mallick, Reduced graphene oxide supported bismuth-Iron mixed oxide nanocomposite: a potent photocatalyst for crystal violet dye degradation and antimicrobial application, J. Photochem. Photobiol. A Chem. 457 (2024) 115912, https://doi.org/10.1016/j.jphotochem.2024.115912.

[7] E. Bailón-García, A. Elmouwahidi, F. Carrasco-Marín, A.F. Pérez-Cadenas, F. J. Maldonado-Hódar, Development of carbon-ZrO2 composites with high performance as visible-light photocatalysts, Appl Catal B 217 (2017) 540–550, https://doi.org/10.1016/j.apcatb.2017.05.090.

[8] R. Ferreira, S. Morales-Torres, L.M. Pastrana-Martinez, F.J. Maldonado-Hódar, J. P. Lourenço, J.M. Silva, I.M. João, M.F. Ribeiro, A. Fernandes, On the characterization and performance of highly dispersed TiO2 nanoparticles onto BEA zeolite in the continuous gas-phase photooxidation of ethylene, RSC Appl. Interfaces (2025), https://doi.org/10.1039/D4LF00286E.

[9] H. Irie, Y. Watanabe, K. Hashimoto, Nitrogen-concentration dependence on photocatalytic activity of TiO2-xNx powders, J. Phys. Chem. B 107 (2003) 5483–5486, https://doi.org/10.1021/jp030133h.

[10] L.T. Pérez-Poyatos, S. Morales-Torres, L.M. Pastrana-Martínez, F.J. Maldonado-Hódar, Sulfur-doped carbon/TiO2 composites for ethylene photo-oxidation. Enhanced performance by doping TiO2 phases with sulfur by mobile species inserted on the carbon support, Catal. Today 446 (2025) 115115, https://doi.org/10.1016/j.cattod.2024.115115.

[11] A.M. Regadera-Macías, S. Morales-Torres, L.M. Pastrana-Martínez, F.J. Maldonado-Hódar, Ethylene removal by adsorption and photocatalytic oxidation using biocarbon –TiO2 nanocomposites, Catal. Today 413–415 (2023) 113932, https://doi.org/10.1016/j.cattod.2022.10.014.

[12] M. Lafjah, F. Djafri, A. Bengueddach, N. Keller, V. Keller, Beta zeolite supported sol–gel TiO2 materials for gas phase photocatalytic applications, J. Hazard. Mater. 186 (2011) 1218–1225, https://doi.org/10.1016/j.jhazmat.2010.11.134.

[13] I.H.A. El Maksod, A. Al-Shehri, S. Bawaked, M. Mokhtar, K. Narasimharao, Structural and photocatalytic properties of precious metals modified TiO2-BEA zeolite composites, molecular, Catalysis 441 (2017) 140–149, https://doi.org/10.1016/j.mcat.2017.08.012.

[14] R. Ferreira, H. Lopes, J.P. Lourenço, J.M. Silva, I.M. João, M.F. Ribeiro, A. Fernandes, Ethylene removal by ag-based ZSM-5 adsorbents for the preservation of climacteric fruits, Microporous Mesoporous Mater. (2024) 113055, https://doi.org/10.1016/j.micromeso.2024.113055.

[15] H. Abdi, H. Maghsoudi, V. Akhoundi, Adsorption properties of ion-exchanged SSZ-13 zeolite for ethylene/ethane separation, Fluid Phase Equilib. 546 (2021) 113171, https://doi.org/10.1016/j.fluid.2021.113171.

[16] L. Cisneros, F. Gao, A. Corma, Silver nanocluster in zeolites. Adsorption of ethylene traces for fruit preservation, Microporous Mesoporous Mater. 283 (2019) 25–30, https://doi.org/10.1016/j.micromeso.2019.03.032.

[17] C. Liu, M. Xin, C. Wang, W. Zhao, Y. Xiang, X. Zhang, L. Qiu, G. Xu, Ag2O nanoparticles encapsulated in ag-exchanged LTA zeolites for highly selective separation of ethylene/ethane, ACS Appl. Nano Mater. 6 (2023) 5374–5383, https://doi.org/10.1021/acsanm.2c05296.

[18] J.D. Monzón, A.M. Pereyra, M.R. Gonzalez, M.S. Legnoverde, M.S. Moreno, N. Gargiulo, A. Peluso, P. Aprea, D. Caputo, E.I. Basaldella, Ethylene adsorption onto thermally treated AgA-zeolite, Appl. Surf. Sci. 542 (2021) 148748, https://doi.org/10.1016/j.apsusc.2020.148748.

[19] Y. Jiang, B. Zhang, X. Jiang, Z. Baolati, B. Zhang, X. Jia, Q. Huang, Metal-loaded starch aerogel for ethylene adsorption under ambient conditions and its preservation of bananas, Chem. Eng. J. 507 (2025) 160731, https://doi.org/10.1016/j.cej.2025.160731.

[20] T.Z. Liza, M.M.H. Tusher, F. Anwar, M.F. Monika, K.F. Amin, F.N.U. Asrafuzzaman, Effect of ag-doping on morphology, structure, band gap and photocatalytic activity of bio-mediated TiO2 nanoparticles, Res. Mater. 22 (2024) 100559, https://doi.org/10.1016/j.rinma.2024.100559.

[21] Y.-C. Liang, C.-C. Wang, C.-C. Kei, Y.-C. Hsueh, W.-H. Cho, T.-P. Perng, Photocatalysis of ag-loaded TiO2 nanotube arrays formed by atomic layer deposition, J. Phys. Chem. C 115 (2011) 9498–9502, https://doi.org/10.1021/jp202111p.

[22] T. Ali, A. Ahmed, U. Alam, I. Uddin, P. Tripathi, M. Muneer, Enhanced photocatalytic and antibacterial activities of ag-doped TiO2 nanoparticles under visible light, Mater. Chem. Phys. 212 (2018) 325–335, https://doi.org/10.1016/j.matchemphys.2018.03.052.

[23] D. Gogoi, A. Namdeo, A.K. Golder, N.R. Peela, Ag-doped TiO2 photocatalysts with effective charge transfer for highly efficient hydrogen production through water splitting, Int. J. Hydrog. Energy 45 (2020) 2729–2744, https://doi.org/10.1016/j.ijhydene.2019.11.127.

[24] S. Zhao, J. Chen, Y. Liu, Y. Jiang, C. Jiang, Z. Yin, Y. Xiao, S. Cao, Silver nanoparticles confined in shell-in-shell hollow TiO2 manifesting efficiently photocatalytic activity and stability, Chem. Eng. J. 367 (2019) 249–259, https://doi.org/10.1016/j.cej.2019.02.123.

[25] R.G. Bansal, J.B. Donnet, F. Stoeckly, Active Carbon, 1st ed., CRC Press, 1988.

[26] P. Makuła, M. Pacia, W. Macyk, How to correctly determine the band gap energy of modified semiconductor Photocatalysts based on UV–vis spectra, J. Phys. Chem. Lett. 9 (2018) 6814–6817, https://doi.org/10.1021/acs.jpclett.8b02892.

[27] A.M. Regadera-Macías, S. Morales-Torres, L.M. Pastrana-Martínez, F.J. Maldonado-Hódar, Optimizing filters of activated carbons obtained from biomass residues for ethylene removal in agro-food industry devices, Environ. Res. 248 (2024) 118247, https://doi.org/10.1016/j.envres.2024.118247.

[28] L.T. Pérez-Poyatos, S. Morales-Torres, L.M. Pastrana-Martínez, F.J. Maldonado-Hódar, The dynamic ethylene adsorption on carbon xerogels as a three-way game between porosity, surface chemistry and humidity, J. Colloid Interface Sci. 678 (2025) 480–493, https://doi.org/10.1016/j.jcis.2024.08.044.

[29] S.M. Al Amin, Md.A. Kowser, Influence of ag doping on structural, morphological, and optical characteristics of sol-gel spin-coated TiO2 thin films, Heliyon 10 (2024) e37558, https://doi.org/10.1016/j.heliyon.2024.e37558.

[30] Y. Shi, Y. Fu, Y. He, J. Zhang, K. Lin, W. Song, X. Yue, D. Wang, A. Wu, C. Tian, Ag-doped hollow multi-shelled structure TiO2 for highly selective photocatalytic CO2 reduction, J. Colloid Interface Sci. 694 (2025) 137684, https://doi.org/10.1016/j.jcis.2025.137684.

[31] G.I. Supelano, F. Mesa, C.A.P. Vargas, J.A.M. Gómez, A. Dussan, Assessment of surface and electrical properties of the TiO2@zeolite hybrid materials, Sci. Rep. 13 (2023) 3650, https://doi.org/10.1038/s41598-023-30529-8.

[32] A.M. Fonseca, I.C. Neves, Study of silver species stabilized in different microporous zeolites, Microporous Mesoporous Mater. 181 (2013) 83–87, https://doi.org/10.1016/j.micromeso.2013.07.018.

[33] E. Sayah, D. Brouri, P. Massiani, A comparative in situ TEM and UV–visible spectroscopic study of the thermal evolution of ag species dispersed on Al2O3 and NaX zeolite supports, Catal. Today 218–219 (2013) 10–17, https://doi.org/10.1016/j.cattod.2013.06.003.

[34] E. Sayah, D. Brouri, Y. Wu, A. Musi, P. Da Costa, P. Massiani, A TEM and UV–visible study of silver reduction by ethanol in ag–alumina catalysts, Appl. Catal. A Gen. 406 (2011) 94–101, https://doi.org/10.1016/j.apcata.2011.08.016.

[35] D.V. Wellia, F. Ardiansyah, A. Lim, S. Arief, R. Subagyo, A.L. Ivansyah, X. Liu, S. Hartati, A.A. Afkauni, L. Zhang, C.S. Tang, X. Yin, C. Diao, M.B.H. Breese, Y. Kusumawati Arramel, Synergistic effects of heteroatom engineering in N-doped TiO2 films probed by X-ray absorption and photoelectron spectroscopy, Surf Interfaces 58 (2025) 105812, https://doi.org/10.1016/j.surfin.2025.105812.

[36] R. Bartolomeu, R. Bértolo, S. Casale, A. Fernandes, C. Henriques, P. da Costa, F. Ribeiro, Particular characteristics of silver species on ag-exchanged LTL zeolite in K and H form, Microporous Mesoporous Mater. 169 (2013) 137–147, https://doi.org/10.1016/j.micromeso.2012.10.015.

[37] J. Shibata, Y. Takada, A. Shichi, S. Satokawa, A. Satsuma, T. Hattori, Ag cluster as active species for SCR of NO by propane in the presence of hydrogen over ag-MFI, J. Catal. 222 (2004) 368–376, https://doi.org/10.1016/j.jcat.2003.11.007.

[38] L. Cisneros, F. Gao, A. Corma, Silver nanocluster in zeolites, adsorption of ethylene traces for fruit preservation, Microporous Mesoporous Mater. 283 (2019) 25–30, https://doi.org/10.1016/j.micromeso.2019.03.032.

[39] J.D. Monzón, A.M. Pereyra, M.R. Gonzalez, M.S. Legnoverde, M.S. Moreno, N. Gargiulo, A. Peluso, P. Aprea, D. Caputo, E.I. Basaldella, Ethylene adsorption onto thermally treated AgA-zeolite, Appl. Surf. Sci. 542 (2021), https://doi.org/10.1016/j.apsusc.2020.148748.

[40] A.M. Pereyra, M.S. Moreno, C.M. Piqueras, J.A. Ávila Ramírez, Ethylene adsorption mechanisms in exchanged zeolite and zeolite-PLA composite for versatile use in climacteric produce preservation, Microporous Mesoporous Mater. 395 (2025) 113702, https://doi.org/10.1016/j.micromeso.2025.113702.

[41] X. Dai, Y. Wang, X. Wang, S. Tong, X. Xie, Polarity on adsorption and photocatalytic performances of N-GR/TiO2 towards gaseous acetaldehyde and ethylene, Appl. Surf. Sci. 485 (2019) 255–265, https://doi.org/10.1016/j.apsusc.2019.04.221.

[42] Y.-H. Wang, S. Bayatpour, X. Qian, B. Frigo-Vaz, P. Wang, Activated carbon fibers via reductive carbonization of cellulosic biomass for adsorption of nonpolar volatile organic compounds, Colloids Surf. A Physicochem. Eng. Asp. 612 (2021) 125908, https://doi.org/10.1016/j.colsurfa.2020.125908.

[43] S. Yamazaki, S. Tanaka, H. Tsukamoto, Kinetic studies of oxidation of ethylene over a TiO2 photocatalyst, J. Photochem. Photobiol. A Chem. 121 (1999) 55–61, https://doi.org/10.1016/S1010-6030(98)00448-1.

[44] A.H. Yonli, I. Gener, S. Mignard, Comparative study of the hydrophobicity of BEA, HZSM-5 and HY zeolites determined by competitive adsorption, Microporous Mesoporous Mater. 132 (2010) 37–42, https://doi.org/10.1016/j.micromeso.2009.08.007.

[45] M. Hussain, N. Russo, G. Saracco, Photocatalytic abatement of VOCs by novel optimized TiO2 nanoparticles, Chem. Eng. J. 166 (2011) 138–149, https://doi.org/10.1016/j.cej.2010.10.040.
[46] G. Zhang, A. Peyravi, Z. Hashisho, Z. Sun, Y. Liu, S. Zheng, L. Zhong, Integrated adsorption and photocatalytic degradation of VOCs using a TiO2/diatomite composite: effects of relative humidity and reaction atmosphere, Catal, Sci. Technol. 10 (2020) 2378–2388, https://doi.org/10.1039/D0CY00168F.
[47] Y. Chen, S. Xu, C. Fang Wen, H. Zhang, T. Zhang, F. Lv, Y. Yue, Z. Bian, Unravelling the role of free radicals in photocatalysis, Chem – A Euro. J. 30 (2024) e202400001, https://doi.org/10.1002/chem.202400001.